



Lithium metal stripping beneath the solid electrolyte interphase

Feifei Shi^a, Allen Pei^a, David Thomas Boyle^b, Jin Xie^a, Xiaoyun Yu^a, Xiaokun Zhang^c, and Yi Cui^{a,d,1}

^aDepartment of Materials Science and Engineering, Stanford University, Stanford, CA 94305; ^bDepartment of Chemistry, Stanford University, Stanford, CA 94305; ^cSchool of Materials and Energy, University of Electronic Science and Technology of China, Chengdu, 611731 Sichuan, People's Republic of China; and ^dStanford Institute for Materials and Energy Sciences, SLAC National Accelerator Laboratory, Menlo Park, CA 94025

Edited by Thomas E. Mallouk, The Pennsylvania State University, University Park, PA, and approved July 3, 2018 (received for review April 21, 2018)

Lithium stripping is a crucial process coupled with lithium deposition during the cycling of Li metal batteries. Lithium deposition has been widely studied, whereas stripping as a subsurface process has rarely been investigated. Here we reveal the fundamental mechanism of stripping on lithium by visualizing the interface between stripped lithium and the solid electrolyte interphase (SEI). We observed nanovoids formed between lithium and the SEI layer after stripping, which are attributed to the accumulation of lithium metal vacancies. High-rate dissolution of lithium causes vigorous growth and subsequent aggregation of voids, followed by the collapse of the SEI layer, i.e., pitting. We systematically measured the lithium polarization behavior during stripping and find that the lithium cation diffusion through the SEI layer is the rate-determining step. Nonuniform sites on typical lithium surfaces, such as grain boundaries and slip lines, greatly accelerated the local dissolution of lithium. The deeper understanding of this buried interface stripping process provides beneficial clues for future lithium anode and electrolyte design.

lithium metal | stripping | solid electrolyte interphase | pitting | battery

To commercially deploy Li-S and Li-O₂ batteries (1–4), numerous studies have been devoted to improving the reversibility of Li metal (2, 5–8). Among them, a major focus has been placed on preventing the growth of lithium dendrites (9–14), which only involves the reduction reaction of Li/Li⁺ redox during the deposition process. Lithium stripping is a crucial process coupled with lithium deposition; however, it has been rarely investigated (15–17). Stripping in lithium metal batteries is the anodic dissolution of lithium. The electrochemical oxidation of its surface atoms results in the liberation of cations into the electrolyte. It involves charge transfer at the interface between lithium and solid electrolyte interphase (SEI), lithium cation migration across the SEI barrier to the SEI/electrolyte interface, and diffusion of solvated ions into electrolyte. In fact, for the majority of Li-metal batteries with cathodes that do not contain lithium, the initial cycle for the anode is stripping, instead of deposition. Furthermore, the morphology/structure of the lithium anode after initial stripping can largely affect the subsequent deposition process (15). Thus, it is particularly important to investigate the widely ignored lithium stripping process with specific emphasis on the Li–SEI interface.

Lithium deposition occurs on the surface of an electrode and generates apparent deposits protruding out of the initial surface, whereas lithium stripping is a subsurface process with features that develop below the Li–SEI interface, making it difficult to probe and characterize. Previous literature has mainly used morphology characterization like optical microscopy, scanning electron microscopy (SEM), or atomic force microscopy (AFM) to check the stripping process (15–17). Although useful information can be extracted with these surficial techniques, they cannot provide an insightful view of the subsurface stripping process. X-ray microtomography has been applied for interface characterization in solid-state lithium batteries (18, 19), but this technique is not ideal for probing early stage stripping due to its

limited resolution. Meanwhile, there are reports that stripping rate affects the cycling efficiency in different electrolytes (20). Some literature reported that higher stripping currents would lead to a smooth Li surface (15), whereas others observed surface cracking during operation at high charging rates (16). Thus, it is vital to clarify the mechanism of lithium stripping and elucidate the factors that influence it.

This study focuses on the mechanism of stripping on metallic lithium anodes under various conditions in both carbonate and ether-based electrolytes. We test the effects of stripping current density on Coulombic efficiency. The lithium stripping process takes place beneath the SEI layer, which makes it hard to observe features from a top view. Here we use a focused ion beam (FIB) to cut fresh cross-sections of stripped lithium electrodes inside a high vacuum chamber (~3E-9 bar). We characterized the stripped cross-section in both the passive and transpassive regions; voids at the lithium–SEI interface and pitting on lithium after SEI layer breakdown were observed. The stripping overpotential and lithium pitting potential have been accurately measured with three-electrode cells. We also explored the effect of impurities, grain boundaries, and slip lines on the lithium stripping process. The present work provides a fundamental understanding of lithium stripping coupled with lithium deposition, which will guide the design of lithium metal anodes in the future.

Significance

This study explores the stripping of lithium anodes under various current densities and in different liquid electrolyte systems. We discovered nanovoid formation between the lithium and the solid electrolyte interphase (SEI). Lithium polarization behavior has been systematically investigated with a three-electrode system and ultramicroelectrode. The diffusion and migration of lithium cations across the SEI have been determined to be the main contributors to the stripping overpotential. Two modes of stripping are proposed based on the passivation condition of lithium: stripping on passivated lithium and pitting on lithium after SEI layer breakdown. The present work provides a mechanistic explanation of Coulombic efficiency decay under high charging current density. We also demonstrate that metallurgical factors greatly accelerate the local dissolution of lithium.

Author contributions: F.S. designed research; F.S., A.P., D.T.B., J.X., X.Y., and X.Z. performed research; and F.S., A.P., and Y.C. wrote the paper.

The authors declare no conflict of interest.

This article is a PNAS Direct Submission.

Published under the PNAS license.

¹To whom correspondence should be addressed. Email: yicui@stanford.edu.

This article contains supporting information online at www.pnas.org/lookup/suppl/doi:10.1073/pnas.1806878115/-DCSupplemental.

Results and Discussion

Stripping Effect on Coulombic Efficiency. High Coulombic efficiency (CE) is the ultimate goal for lithium anodes in Li-based batteries. However, it is still not clear how to correlate the stripping process with CE. To isolate this process, we deposited $0.5 \text{ mA}\cdot\text{cm}^{-2}$ lithium at a fixed current of $0.2 \text{ mA}\cdot\text{cm}^{-2}$ and then stripped the deposited lithium at varied currents of 0.1, 0.5, 1, 3, and $5 \text{ mA}\cdot\text{cm}^{-2}$. Here we use two different methods to measure the CE. The first method is the frequently reported Li||Cu setup (21). In this method, the Cu electrode was discharged to 0 V vs. Li/Li⁺ by applying $0.5 \text{ mA}\cdot\text{cm}^{-2}$ current then charged back to 1 V at $0.5 \text{ mA}\cdot\text{cm}^{-2}$ for 10 cycles to initialize the formation of the SEI and remove surface impurities without Li metal deposition. As shown in Fig. 1 *A* and *B*, lithium cycling in both EC/DEC and DOL/DME/LiNO₃ exhibits a trend of lower CE with increased stripping current density. However, stripping current has a less pronounced effect on the CE in DOL/DME/LiNO₃ electrolyte. This may be related to the severe dendrite growth on the lithium side in EC/DEC electrolyte. The noisy data points at $5 \text{ mA}\cdot\text{cm}^{-2}$ in Fig. 1 *A* and *B* are also related to these effects. To reduce/eliminate the polarization and growth of dendrites at the lithium counter electrode during high stripping currents, we use a lithium-free method to measure the CE. Zhang and coworkers (20) first reported using a Cu||LiFePO₄ cell to accurately measure the CE. Here we use a precycled Li₄Ti₅O₁₂ (LTO) electrode as the lithium source. The first three cycles of the LTO lithiation/delithiation and CE measurement protocol are shown in *SI Appendix, Fig. S1*, with more details described in *SI Appendix, SI Materials and Methods*. Due to the low polarization (22) and high reversibility of LTO in both EC/DEC and DOL/DME/LiNO₃ electrolytes, the Cu||LTO cells have a much more stable trend of CE evolution in Fig. 1 *C* and *D*. Even after excluding the factors of electrode polarization and dendrite growth on the counter electrode, higher stripping currents still result in poorer CEs in EC/DEC electrolyte, in contrast to results from high concentration electrolytes (20, 23). DOL/DME/LiNO₃ electrolyte shows

a more stable CE with variable current density. The potential–capacity profiles corresponding to Fig. 1 have been extracted in *SI Appendix, Fig. S2*. We observed obvious increases in stripping overpotential in both setups. Due to the limitations of the two-electrode system, the absolute value of overpotential could be influenced by the counter electrode polarization. To elucidate the role of the stripping reaction on the reversibility of lithium in different electrolytes, we explore the stripping mechanism in the following sections.

Stripping on Passivated Lithium. Various anodic dissolution mechanisms exist for metals, depending on the range of applied potential with respect to their passivation condition. Due to the low chemical potential of lithium, all electrolytes will react with it and lead to a spontaneous passivation layer, i.e., SEI. We will first discuss the most common case of stripping on lithium: stripping with SEI. To eliminate any artificial effect on the interface, we generated lithium electrodes where half of the sample surface was stripped and the other half was pristine. In this way, we could fairly compare the reacted vs. unreacted area. More discussion about the possible ion beam damage issue has been provided in *SI Appendix, Cross-Section Morphology Characterization*. Custom half-blocked separators were used to cover and prevent part of the lithium surface from electrochemically reacting as shown in Fig. 2 *A* and *B*. More details about the separator are given in *SI Appendix, Fig. S3*. As shown in Fig. 2*C*, there is an obvious contrast between the stripped and nonreacted regions in the Ga⁺ ion image; this contrast arises from the density difference beneath the surface. However, in the secondary electron image, there is almost no difference in the surface morphology between the two regions (*SI Appendix, Fig. S3B*). Fig. 2 *D* and *G* show the cross-section of the lithium electrode with half-blocked separator before any cycling; we find there is a uniform film across the blocking boundary, attributed to the combination of SEI and residual electrolyte. Attenuated total reflection–Fourier transform infrared measurement has been conducted to characterize the SEI (24–26). In *SI Appendix, Fig. S4*, the composition of SEI on the stripped lithium shows no difference compared with that on the electrodeposited lithium (27). Due to their electronic conductivity difference, the bulk lithium can be distinguished from the above film in the secondary electron images. In the coin cell configuration, the large mechanical pressure deforms Li metal foil on the separator. Different separator thicknesses from the blocked side (20 μm) to the unblocked side (25 μm) lead to a height difference on lithium metal across the boundary (~2.5 μm). Fig. 2 *E, F, H, and I* and *SI Appendix, Fig. S5*, show the interface after stripping in DOL/DME 1 M LiTFSI, 1% LiNO₃ electrolyte at current densities of 0.5, 2, and $1 \text{ mA}\cdot\text{cm}^{-2}$. We observe a string of gradually formed voids located between the SEI layer and pristine lithium. In addition, larger current densities cause larger sizes of voids. Similar trends are observed in EC/DEC 1 M LiPF₆ electrolyte as shown in *SI Appendix, Fig. S6*. We believe that the voids at the lithium/SEI interface (Fig. 2 and *SI Appendix, Fig. S6*) are attributed to the piling up of accumulated lithium vacancies. This is consistent with the point defect model for metal dissolution with a passivation layer developed by Macdonald and coworkers (28, 29). After lithium cations migrate through the SEI layer, the metal vacancies will be left at the interface between lithium and the SEI layer. These lithium metal vacancies typically tend to submerge into the bulk of lithium and hence disappear from the surface. However, when the rate of cation extraction is higher than the rate of vacancy submergence, these vacancies accumulate at the lithium/SEI interface and lead to a local concentration of vacancies, i.e., voids. The fate of these voids is quite critical for lithium stripping because their aggregation can lead to the formation of big cavities at the lithium/SEI interface, which is detrimental for the adherence/passivity of the SEI layer.

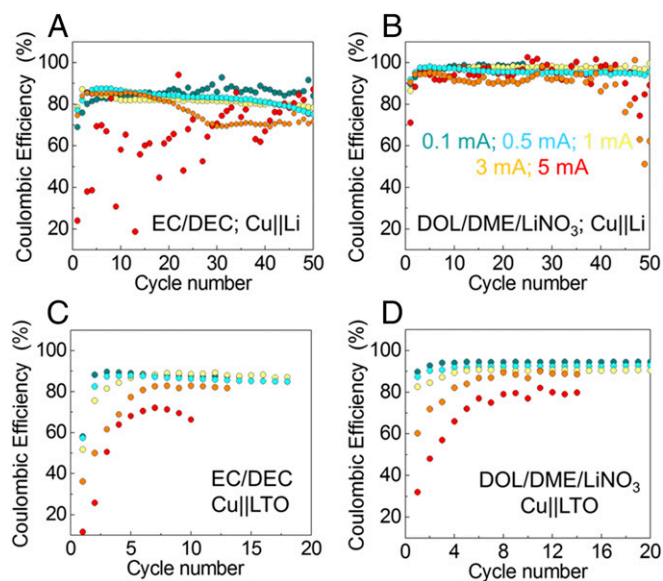


Fig. 1. Coulombic efficiency dependence on stripping current density in different electrolyte systems. Cu||Li setup for (A) EC/DEC 1 M LiPF₆ and (B) DOL/DME 1 M LiTFSI, 1% LiNO₃. Lithium-free Cu||LTO setup for (C) EC/DEC 1 M LiPF₆ and (D) DOL/DME 1 M LiTFSI, 1% LiNO₃. For each setup, we deposited $0.5 \text{ mA}\cdot\text{cm}^{-2}$ lithium at a fixed current of $0.2 \text{ mA}\cdot\text{cm}^{-2}$ and stripped lithium at currents of 0.1, 0.5, 1, 3, and $5 \text{ mA}\cdot\text{cm}^{-2}$. Each condition has been repeated more than twice.

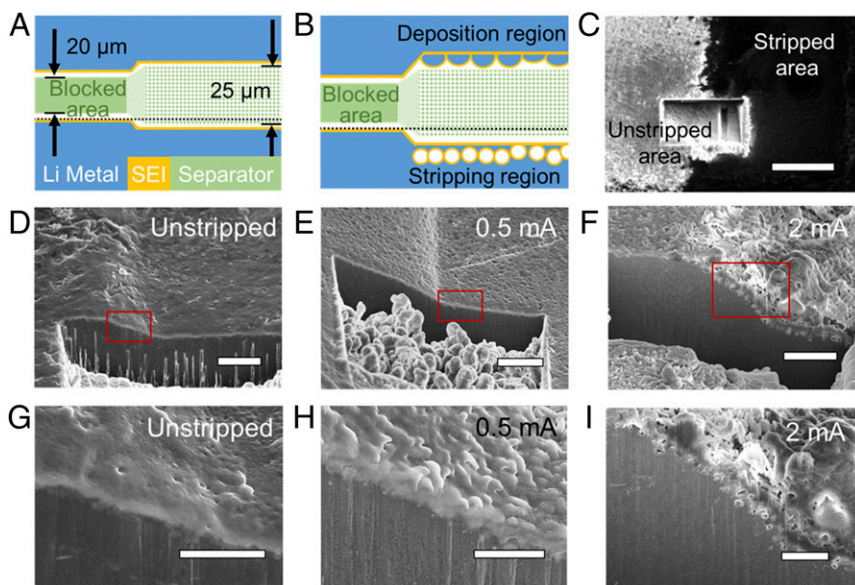


Fig. 2. Lithium stripping in DOL/DME 1M LiTFSI, 1% LiNO₃ electrolyte. Schematic of half-blocked coin cell (A) before charging and (B) after first charging; (C) Ga-ion image at the boundary between unstripped and stripped area; and secondary electron images of cross-section on Li foil (D and G) without cycling, (E and H) after stripping at 0.5 mA·cm⁻², and (F and I) after stripping at 2 mA·cm⁻². The red boxes indicate the zoomed-in regions. All of the stripping capacities are 1 mAh·cm⁻². (Scale bars: C, 20 μm; D–F, 5 μm; G and I, 2.5 μm; and H, 1.5 μm.)

Pitting on Lithium After Breakdown of the SEI Layer. High-rate electrochemical dissolution of lithium may lead to a vigorous growth of voids, which causes a local collapse of SEI layer. Subsequently, the breakdown site reacts much faster than other areas on the surface, thereby leading to pit growth. In this section, we discuss the pitting on lithium after SEI layer breakdown as a second type of stripping. Fig. 3 shows the lithium pitting in EC/DEC 1 M LiPF₆ electrolyte at various current densities. From top-view images (Fig. 3 A, E, and I), the total area coverage of pits increases as the current density increases. By using the FIB to directly observe the cross-section of the pitting area (Fig. 3 C, G, and K), we find that the depth of pits decreases as current density increases (6.6 μm for 1 mA·cm⁻², 5.4 μm for 5 mA·cm⁻², and 4.3 μm for 10 mA·cm⁻²). This is consistent with volume conservation because the same capacity of lithium is stripped in each case. More pitting results from experiments with the DOL/DME/LiNO₃ electrolyte are provided in *SI Appendix, Fig. S7*. We found that the initiation of pitting barely occurs until the current reaches 5 mA·cm⁻² in DOL/DME LiNO₃ electrolyte, which is consistent with its good CE under high current density in Fig. 1. The voids appear at the bottom of the pit, between the interface of lithium and SEI layer (Fig. 3 D, H, and L), which is similar to the voids in Fig. 2. This validates the model that pit initiation is caused by the collapse of accumulated voids (28). In addition, the decreasing pit area with increasing applied current density may be related to the kinetics of void generation. At a large current density, the rate of void initiation could be very fast and dominate the rate of void agglomeration, resulting in more shallow pits. This trend is true for both types of electrolyte. To determine the origin of different stripping modes on lithium, we will discuss and compare the stripping overpotential and pitting potential in the next two sections.

Overpotentials of Stripping. As shown in the previous results, different current densities give much different CEs and interface morphologies. Here we test the polarization behavior of lithium stripping. Fig. 4 A and B show the stripping polarization in EC/DEC and DOL/DME/LiNO₃ electrolyte with a three-electrode cell. To accurately measure the potentials in the different electrolyte/SEI systems, a precycled LTO electrode is used as the reference electrode (22). The thickness of freshly formed SEI layers on lithium will greatly change within the first few hours (17). To elucidate the effect of SEI thickness, each lithium foil is rested in the electrolyte for more than 10 h. More details about

the polarization measurement are stated in *SI Appendix, SI Materials and Methods*. We observe a much larger overpotential during stripping in EC/DEC electrolyte compared with that in DOL/DME with the same current density, which is consistent with the literature (17, 30). The overpotential of stripping is mainly attributed to charge transfer, diffusion, and iR drop (31). We use fast polarization scans (scan rate of 200 mV·s⁻¹) with a tungsten microelectrode (diameter of 25 μm) to investigate the electron transfer process on the lithium surface. This fast potentiodynamic measurement makes the speed of Li deposition much faster than that of lithium corrosion, such that only the contribution of electron transfer is significant (27, 32). More experimental details are stated

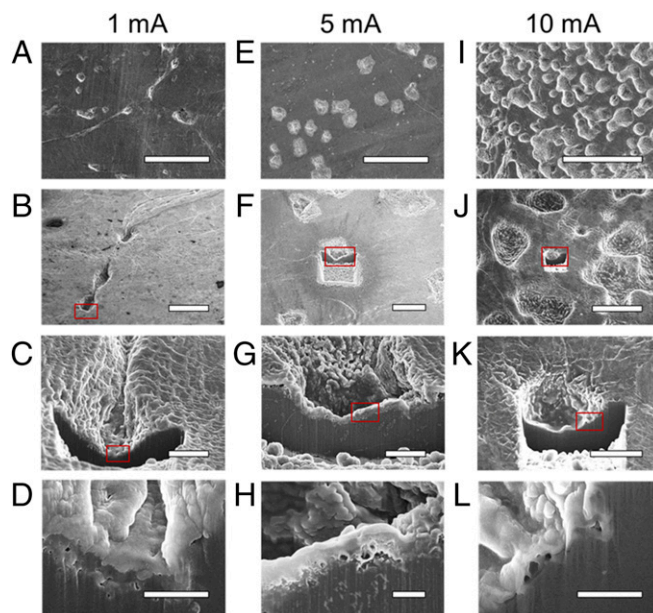


Fig. 3. Lithium pitting at various current densities in EC/DEC 1M LiPF₆ electrolyte. Stripping at current density of (A–D) 1 mA·cm⁻², (E–H) 5 mA·cm⁻², and (I–L) 10 mA·cm⁻². All of the cross-section images are taken at a tilt angle of 52°; the stripped capacity is 1 mAh·cm⁻². The red boxes indicate the zoomed-in regions. (Scale bars: A, E, and I, 100 μm; B, F, and J, 20 μm; C, G, and K, 4 μm; and D, H, and L, 1 μm.)

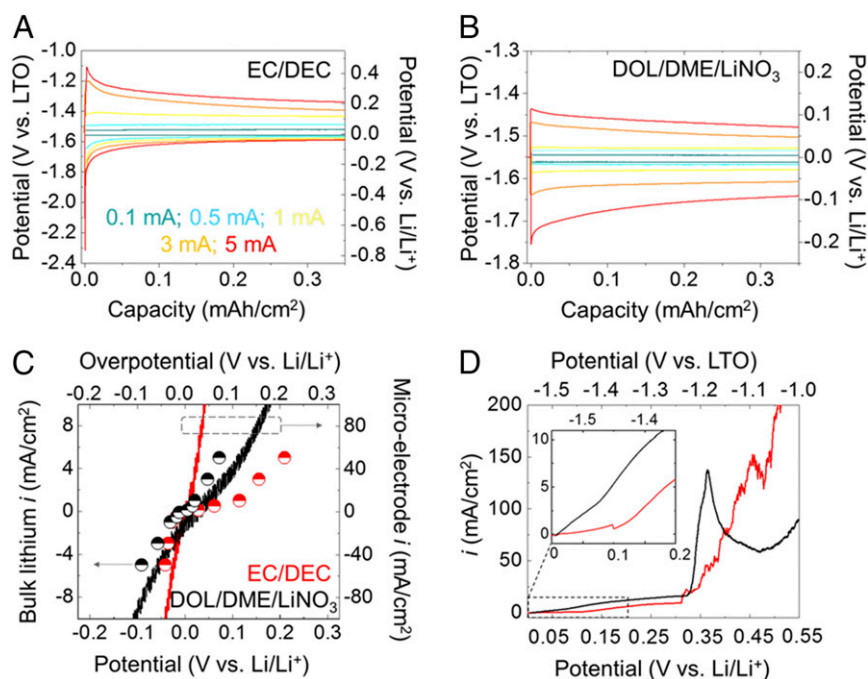


Fig. 4. Polarization behavior of lithium during stripping. Galvanostatic tests under current densities of 0.1, 0.5, 1, 3, and 5 mA·cm⁻² in (A) EC/DEC 1 M LiPF₆ and (B) DOL/DME 1 M LiTFSI, 1% LiNO₃. (C) Comparison of the polarization between the microelectrode method (line curves) measured on SEI-free lithium and the galvanostatic method (points) measured on lithium with SEI at the capacity of 0.35 mAh·cm⁻². (D) Anodic polarization curves for lithium foil with SEI, scan rate 1 mV·s⁻¹. (Inset) A magnified plot of the polarization curve in the low overpotential region. Red lines/dots indicate measurements in EC/DEC 1 M LiPF₆, and black lines/dots indicate measurements in DOL/DME 1 M LiTFSI, 1% LiNO₃. To form a stable SEI film on lithium, a 10-h resting process is applied to each bulk lithium electrode.

in *SI Appendix, Measurement of Microelectrode*. Fig. 4C shows the polarization curve measured with a microelectrode and bulk lithium electrode (SEI preformation treatment, 10 h aging). When electron transfer is the rate-determining step, the Li deposition/stripping reaction in EC/DEC electrolyte (red line) has higher exchange current density and thus smaller polarization compared with that in the DOL/DME electrolyte (the black line). However, the stabilized stripping overpotentials of Li foil (taken from Fig. 4A and B) with SEI layer show the opposite trend (red and black dots). Hence, electron transfer is not the dominating factor for the stripping overpotential when the lithium surface is covered with the SEI layer.

During stripping and after the electron transfer step, lithium cations must migrate across the SEI barrier to the SEI/electrolyte interface. When the transportation of cations through the SEI is the rate-determining step, a concentration gradient of Li⁺ will form across the SEI layer. Rapid metal dissolution at large overpotentials will cause saturation and precipitation of salt at the lithium/SEI interface (33). The overpotential from the diffusion-limited current in SEI can be calculated by the equation below, where c_s is the concentration of saturation and d_N is the thickness of the Nernst diffusion layer in front of an electrode (33):

$$\eta_D = \frac{RT}{nF} \ln \left(\frac{i_D + i}{i_D} \right); i_D = \frac{nFDc_s}{d_N}$$

Thus, the ionic conductivity of the SEI and saturation concentration of lithium cations within the SEI determines the diffusion overpotential contribution. An artificial SEI with properly designed properties (i.e., high ionic conductivity, high lithium solubility, and compositional uniformity) could largely suppress the stripping overpotential. Electrochemical impedance spectroscopy (EIS) in *SI Appendix, Fig. S8*, shows that the SEI layer in DOL/DME/LiNO₃ has a much smaller interfacial impedance compared

with that of EC/DEC, which reflects the higher ionic conductivity of the SEI formed in DOL/DME/LiNO₃ electrolyte. This explains why the lithium foil in DOL/DME/LiNO₃ is less polarized, and less pitting behavior exists. The iR drop potential can also be extracted from the EIS data (*SI Appendix, Fig. S8*). We note that the interphase impedance (1050 Ω for EC/DEC and 98 Ω for DOL/DME/LiNO₃) is far larger than that of the electrolyte resistance (1.1 Ω for EC/DEC and 0.7 Ω for DOL/DME/LiNO₃), indicating that ionic transport through the SEI is the dominating factor in the overpotential of stripping.

Pitting Potential. Pitting phenomena initiate when the applied potential exceeds a critical value and current density sharply increases. This critical potential is called the pitting potential, which differentiates metallic dissolution in the passive state or in the pitting state (33). To determine the onset potential of pitting, we measure anodic polarization curves of lithium foil with a three-electrode cell at a scan rate of 1 mV·s⁻¹. Fig. 4D shows the stripping current density drastically increases during the positive scan. Considering the previous results in Figs. 3 and 4A and B and *SI Appendix, Fig. S7*, we determined that the onset potential of pitting is around 0.1 V vs. Li/Li⁺ in both EC/DEC and DOL/DME electrolyte. Due to the large polarization response of lithium in EC/DEC electrolyte, the stripping overpotential reaches the pitting potential at a current density of 1 mA·cm⁻² (Fig. 3A–D). In DOL/DME/LiNO₃ electrolyte, the stripping overpotential of lithium does not exceed the pitting potential until 5 mA·cm⁻², which explains the drop of CE at 5 mA in Fig. 1D. Thus, by comparing the stripping overpotential and the pitting potential, we can easily determine whether pitting will initiate, which is vital for the identification of stripping modes.

Metallurgical Factors Influencing the Lithium Stripping Process.

Impurities. Upon characterization of pristine lithium foil, we observed impurity crystals embedded inside the bulk. The

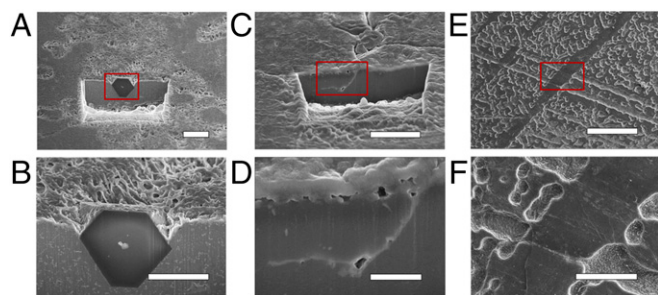


Fig. 5. Effect of metallurgical nonuniformity on the lithium stripping. (A and B) Lithium foil with an impurity crystal after being stripped in DOL/DME/LiNO₃ at current density of 10 mA·cm⁻². (C and D) Lithium foil with grain boundary after being stripped in EC/DEC 1 M LiPF₆ at current density of 0.5 mA·cm⁻². (E and F) Lithium foil with slip lines after being stripped in EC/DEC 1 M LiPF₆ at current density of 10 mA·cm⁻². The red boxes indicate the zoomed-in regions. (Scale bars: A, 10 μm; B and C, 5 μm; D, 1 μm; E, 200 μm; and F, 50 μm.)

FIB–energy-dispersive X-ray result shows that the major composition of the impurity is oxygen, although it could not detect lithium due to the low Z. Thus, we identify the impurity as Li₂O (SI Appendix, Fig. S9), as reported in the literature (12). However, unlike the stripping process in the solid electrolyte case, we did not observe any accelerated void formation below the impurity particle in liquid electrolyte, as shown in Fig. 5 A and B. This could be attributed to the poor conductivity of both electrons and ions inside such a large impurity particle (~10 μm), which prevents any reaction electron/ion flux from penetrating through it. The higher-ionic conductivity environment in the liquid electrolyte system can more easily redistribute lithium ion flux than that of the solid electrolyte. Thus, the oxygen-containing impurity from manufacturing plays a less important role than expected.

Grain boundaries. Metals are usually crystalline materials, and their structure has a strong influence on the dissolution reaction. We know that commercial lithium foil has strong texture along the (100) plane, and thus, the grains with similar orientation on the lithium will have similar dissolution speed (27). Lattice diffusion represents the most severe constraint to atomic migration, which leads to poor atomic diffusivity. The diffusivity of lithium atoms (⁷Li) in solid lithium metal (⁷Li) at 25 °C is a low value of 5.5E-11 cm²·s⁻¹ (34). In contrast, grain boundaries enable fast atomic diffusion of lithium because they have less densely packed structure. Moreover, solvent molecules are also able to diffuse into these boundaries and form

SEI layers. Lithium ion diffusion in SEI is usually faster than the lithium atom diffusion through its lattice. Model SEI (Li₂CO₃) has a diffusivity as high as 1.1E-7 cm²·s⁻¹ (35). Thus, these grain boundaries provide the most prominent high-diffusivity paths for both lithium atoms and lithium ions. Fig. 5 C and D shows a grain boundary in a lithium foil after cycling in EC/DEC 1 M LiPF₆ at a current density of 0.5 mA·cm⁻². A string of voids is observed along the grain boundary, which is far below the interface of the bulk (~2 μm). The existence of such a grain boundary largely affects the frontier boundary of lithium ion consumption, which will influence the uniformity of the stripping process.

Slip lines. Metal surfaces are heterogeneous. Besides the grain boundaries, there are atomic surface structures with step, kink, and ad-sites on a terrace. During active dissolution, atoms are removed from the crystal lattice and passed into solution as solvated ions. This process does not occur uniformly all over the surface but instead at energetically favorable sites, like low-index surfaces or kink sites (33). Roll pressing normally generates slip lines on the lithium foil (SI Appendix, Fig. S10A). After stripping, we find that pitting preferentially takes place along those slip lines (Fig. 5 E and F). Previous literature also described similar phenomenon, but they described slip lines as giving “cracked surfaces” and discussed them as grain boundaries (15). However, in our results, we find that the slip lines behave like neither surface cracks nor grain boundaries. The cross-section characterization of slip line sites (SI Appendix, Fig. S10B–D) shows that on the slip line, there is an evenly distributed passivation layer. There are no signs of any surface cracks or seam-like structures like those at grain boundaries. The roll-pressing treatment actually generates steps and kinks on the crystal grains of lithium surface. The step height difference along slip lines is around 500 nm (SI Appendix, Fig. S10D), and the passivation layer on kink sites is slightly thicker than that of the step. Hence, we believe that the preferential stripping along slip lines is due to the fast reaction speed of lithium atoms at the kink sites on those lines. This explains why the lithium surface does not react homogeneously, and instead, preferential dissolution of some sites occurs.

Stripping Mechanism Summary. We have discussed two types of stripping: stripping on passivated lithium and pitting on lithium after SEI layer breakdown (Fig. 6). Stripping usually initiates with the first mode, stripping from beneath the intact passivation layer. During the initial stripping, the lithium cations migrate through the passive layer to the electrolyte. The leftover metal vacancies accumulate at the metal–passivation layer interface

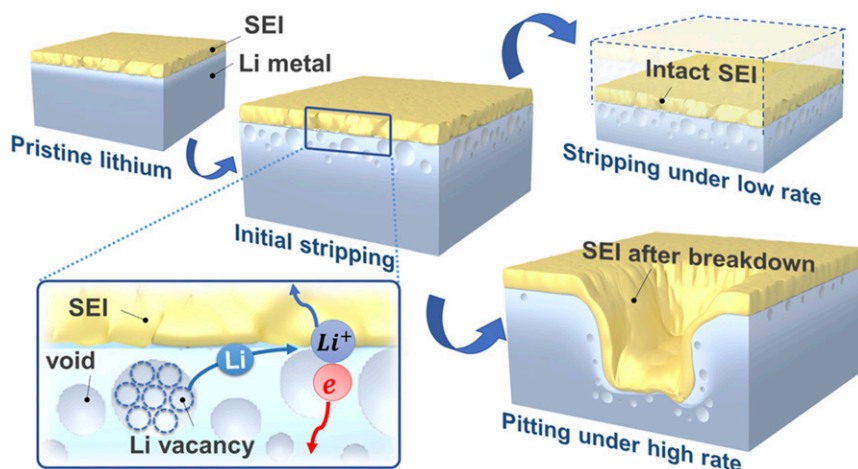


Fig. 6. Evolution of lithium electrode under different stripping conditions.

and finally lead to a local void. Under high-rate electrochemical dissolution, the vigorous growth of voids causes a local collapse of the SEI layer. The breakdown of the SEI layer marks the transition to the other stripping mode, i.e., pitting. By comparing the stripping overpotential and the pitting potential, we can determine the stripping mode. The overpotential of stripping is mainly caused by lithium cation transportation through the SEI. The ionic conductivity and saturation concentration of lithium cations within the SEI may affect the formation speed of vacancies and hence the thickness of the void layer at the lithium/SEI interface.

Conclusion

This work examines the mechanism of stripping on a lithium anode under various conditions in both carbonate and ether-based electrolytes. We visualized the formation of voids at the interface of lithium/SEI after stripping in each liquid electrolyte system. Under high charge rates, the fast accumulation of voids at the interface of lithium/SEI leads to the collapse of the SEI layer, which marks the initiation of its pitting. We systematically measured the static and fast potentiodynamic polarization behavior on both bulk lithium and tungsten microelectrode, finding that the lithium cation diffusion through the SEI layer is mainly responsible for the differences in stripping overpotential. Metallurgical nonuniformity effects on stripping have also been explored. We evaluated effects from impurities, grain boundaries, and slip lines. Both grain boundaries and slip lines will largely aggravate the nonuniformity of stripping on the lithium surface. The present mechanistic analysis will guide further optimization of the lithium anode, including minimization of interfacial voids, enhancement of ionic conductivity in the SEI layer, and improvement of the manufacturing process of lithium anodes for better metallurgical uniformity.

Materials and Methods

Materials. The 2032-type coin cells with copper or stainless steel working electrodes and Li foil (Alfa Aesar) counter/reference electrodes were assembled in an argon-filled glove box (MB-200B; Mbraun). A double-stacked commercial separator (2325; Celgard) was used between the two electrodes, and 30 μL of electrolyte was added to each cell. The electrolyte was 1 M LiPF_6 /ethylene carbonate (EC):diethyl carbonate (DEC) (1:1 vol/vol) (Novolyte Technologies, BASF). The 1,3-dioxolane/1,2-dimethoxyethane (DOL/DME, 1:1 vol/vol) (Sigma-Aldrich) with 1 M lithium bis(trifluoromethylsulfonyl)imide (LiTFSI) (Solvay S.A.) with 1 wt % LiNO_3 (Sigma-Aldrich) as an additive was used as the electrolyte. Electrolyte salts were dried at 100 $^\circ\text{C}$ for over 24 h in Ar atmosphere. Dimethyl carbonate (DMC) (Aldrich, 99.9+%, HPLC grade) was used as rinsing solvent.

Three-Electrode Swagelok Cell. A three-electrode Swagelok cell was used for polarization experiments. Lithium foil is applied as both working and counter electrode. To eliminate the drift of Li/Li^+ potential in various electrolyte systems and normalize the polarization comparison, the reference electrode is a precycled $\text{Li}_4\text{Ti}_5\text{O}_{12}$ electrode with C/5 rate (SI Appendix, Fig. S1A). Due to the reactivity of lithium, a 10-h resting process is applied to all lithium electrodes. This aging time has been chosen based on time-dependent impedance spectroscopy (SI Appendix, Fig. S5).

Cross-Section Morphology Characterization. After electrochemical treatment, the lithium samples were gently rinsed in DMC or DOL to remove residual electrolyte. The samples were then transferred to a dual beam FIB-scanning electron microscope (Helios NanoLab 600i, FEI) for imaging. The samples are loaded on the sample stage and sealed in an Ar-filled pouch bag before transfer into the vacuum chamber. The accelerating voltage for the Ga^+ ion source is 30 kV, and milling current is 2.5 nA. The SEM images are taken at the accelerating voltage of 5 kV.

ACKNOWLEDGMENTS. The work was supported by the Assistant Secretary for Energy Efficiency and Renewable Energy, Office of Vehicle Technologies, of the US Department of Energy under the Battery Materials Research program and Battery 500 Consortium program. A.P. acknowledges support by the Stanford Graduate Fellowship. X.Z. acknowledges the National Science Funds of China (Contract 51472044) and Program for New Century Excellent Talent in University (Contract NCET-12-0098).

- Bruce PG, Freunberger SA, Hardwick LJ, Tarascon J-M (2011) Li-O₂ and Li-S batteries with high energy storage. *Nat Mater* 11:19–29.
- Sun Y, Liu N, Cui Y (2016) Promises and challenges of nanomaterials for lithium-based rechargeable batteries. *Nat Energy* 1:16071.
- Lu J, et al. (2014) Aprotic and aqueous Li-O₂ batteries. *Chem Rev* 114:5611–5640.
- Peng Z, Freunberger SA, Chen Y, Bruce PG (2012) A reversible and higher-rate Li-O₂ battery. *Science* 337:563–566.
- Aurbach D, et al. (2002) Attempts to improve the behavior of Li electrodes in rechargeable lithium batteries. *J Electrochem Soc* 149:A1267–A1277.
- Xu W, et al. (2014) Lithium metal anodes for rechargeable batteries. *Energy Environ Sci* 7:513–537.
- Aurbach D, Zinigrad E, Teller H, Dan P (2000) Factors which limit the cycle life of rechargeable lithium (metal) batteries. *J Electrochem Soc* 147:1274–1279.
- Lin D, Liu Y, Cui Y (2017) Reviving the lithium metal anode for high-energy batteries. *Nat Nanotechnol* 12:194–206.
- Yan K, et al. (2016) Selective deposition and stable encapsulation of lithium through heterogeneous seeded growth. *Nat Energy* 1:16010.
- Li W, et al. (2015) The synergistic effect of lithium polysulfide and lithium nitrate to prevent lithium dendrite growth. *Nat Commun* 6:7436.
- Lu Y, Tu Z, Archer LA (2014) Stable lithium electrodeposition in liquid and nanoporous solid electrolytes. *Nat Mater* 13:961–969.
- Zhao J, et al. (2017) Surface fluorination of reactive battery anode materials for enhanced stability. *J Am Chem Soc* 139:11550–11558.
- Zhang J-G, Xu W, Henderson WA (2016) *Lithium Metal Anodes and Rechargeable Lithium Metal Batteries* (Springer, Cham, Switzerland).
- Qian J, et al. (2015) High rate and stable cycling of lithium metal anode. *Nat Commun* 6:6362.
- Gireaud L, Grugeon S, Laruelle S, Yrieix B, Tarascon J-M (2006) Lithium metal stripping/plating mechanisms studies: A metallurgical approach. *Electrochem Commun* 8:1639–1649.
- Cohen YS, Cohen Y, Aurbach D (2000) Micromorphological studies of lithium electrodes in alkyl carbonate solutions using in situ atomic force microscopy. *J Phys Chem B* 104:12282–12291.
- Wood KN, et al. (2016) Dendrites and pits: Untangling the complex behavior of lithium metal anodes through operando video microscopy. *ACS Cent Sci* 2:790–801.
- Harry KJ, Hallinan DT, Parkinson DY, MacDowell AA, Balsara NP (2014) Detection of subsurface structures underneath dendrites formed on cycled lithium metal electrodes. *Nat Mater* 13:69–73.
- Harry KJ, Liao X, Parkinson DY, Minor AM, Balsara NP (2015) Electrochemical deposition and stripping behavior of lithium metal across a rigid block copolymer electrolyte membrane. *J Electrochem Soc* 162:A2699–A2706.
- Qian J, et al. (2016) Anode-free rechargeable lithium metal batteries. *Adv Funct Mater* 26:7094–7102.
- Pei A, Zheng G, Shi F, Li Y, Cui Y (2017) Nanoscale nucleation and growth of electrodeposited lithium metal. *Nano Lett* 17:1132–1139.
- Mantia FL, Wessells CD, Deshazer HD, Cui Y (2013) Reliable reference electrodes for lithium-ion batteries. *Electrochem Commun* 31:141–144.
- Zheng J, et al. (2016) Highly stable operation of lithium metal batteries enabled by the formation of a transient high-concentration electrolyte layer. *Adv Energy Mater* 6:1502151.
- Shi F, et al. (2015) A catalytic path for electrolyte reduction in lithium-ion cells revealed by in situ attenuated total reflection-Fourier transform infrared spectroscopy. *J Am Chem Soc* 137:3181–3184.
- Shi F, et al. (2014) Identification of diethyl 2,5-dioxahexane dicarboxylate and polyethylene carbonate as decomposition products of ethylene carbonate based electrolytes by Fourier transform infrared spectroscopy. *J Phys Chem C* 118:14732–14738.
- Shi F, Ross PN, Somorjai GA, Komvopoulos K (2017) The chemistry of electrolyte reduction on silicon electrodes revealed by in situ ATR-FTIR spectroscopy. *J Phys Chem C* 121:14476–14483.
- Shi F, et al. (2017) Strong texturing of lithium metal in batteries. *Proc Natl Acad Sci USA* 114:12138–12143.
- Macdonald DD (1992) The point defect model for the passive state. *J Electrochem Soc* 139:3434–3449.
- Chao CY, Lin LF, Macdonald DD (1981) A point defect model for anodic passive films: I. Film growth kinetics. *J Electrochem Soc* 128:1187–1194.
- Bieker G, Winter M, Bieker P (2015) Electrochemical in situ investigations of SEI and dendrite formation on the lithium metal anode. *Phys Chem Chem Phys* 17:8670–8679.
- Bard AJ, Faulkner LR (2001) *Electrochemical Methods: Fundamentals and Applications* (John Wiley & Sons, Inc., New York), 2nd Ed.
- Aurbach D (1999) *Nonaqueous Electrochemistry* (Marcel Dekker, Inc., New York).
- Macdonald P (2012) *Corrosion Mechanisms in Theory and Practice* (Taylor & Francis Group, Boca Raton, FL).
- Lodding A, Mundy JN, Ott A (1970) Isotope inter-diffusion and self-diffusion in solid lithium metal. *Phys Status Solidi* 38:559–569.
- Shi S, et al. (2012) Direct calculation of Li-ion transport in the solid electrolyte interphase. *J Am Chem Soc* 134:15476–15487.